Local Actuation of Tubular Origami

S. W. Grey, F. L. Scarpa, M. Schenk

Abstract: *This paper is an experimental and numerical investigation of the elastic decay of localised actuation in a tubular engineering origami system. A numerical model of a Miura-ori tube subject to localised actuation is developed, using experimentally determined material properties, and verified by comparing against a locally actuated experimental model. Results indicate that the ratio between the facet and folds stiffness influences the distance over which localised actuation decays in Miura-ori tubes. Furthermore, a 'spring-back' effect is observed where an actuation causes an opposite sense deformation further along the tube.*

1 Introduction

Origami promises the ability to achieve three-dimensional geometries from flat sheets of material. In order to achieve this, origami-inspired systems could be designed with distributed embedded actuators, allowing the shape to be controlled through a combination of local actuations. A crucial constraint to the development of such systems is the current understanding of the propagation of local actuation in origami systems. The current work focuses on Miura-ori tubes [Filipov et al. 15] with the aim of simplifying the propagation of an actuation to a single direction, along the length of the tube.

Engineering origami structures are not restricted to rigid-foldable mechanisms with a single degree of freedom, such as the Miura-ori pattern. For instance, patterns that are developable, but not rigid-foldable, have been used to generate complex 3D shapes or introduce multistability [Dudte et al. 16, Silverberg et al. 15]. In this paper we focus on rigid-foldable patterns which also experience deformations between the fold lines, due to the nature of the loading.

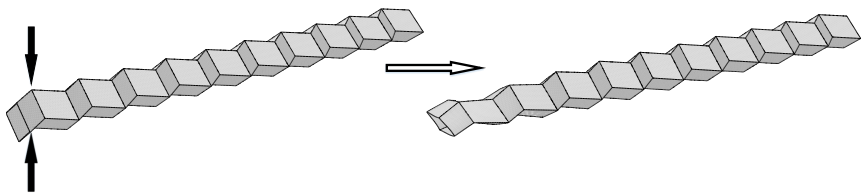

Figure 1: *A localised actuation, here compressing a unit cell, at one end of the Miura-ori tube propagates along its length. The effect decays away from the source, eventually returning to the unperturbed shape. This elastic decay is a result of facet deformations, which alter the unit cell kinematics.*

Using the simplest model to capture the mechanics of origami, rigid origami [Tachi 09], the Miura-ori pattern has a single degree of freedom. This drives the kinematic models that capture the global behaviours of Miura-ori sheets [Schenk and Guest 13, Wei et al. 13]. However, folds are not perfect hinges, and introducing a folding stiffness transforms the Miura-ori from a mechanism into a structure. Furthermore, in physical structures the facets have a finite stiffness and can, therefore, deform. This effectively increases the number of degrees of freedom at the vertices, and introduces an elastic decay of any actuation. Figure 1 shows a representative actuation of a Miura-ori tube, achieved by compressing the left most unit cell; the actuation has a reduced effect in each unit cell until eventually returning to the undeformed shape. This elastic decay is due to deformations between the fold lines, which rigid origami cannot capture. The aim of this paper is to better understand this elastic decay, and the influence of the elastic properties of the folds and facets on the decay.

Finite Element Analysis (FEA) may be used to investigate the physical behaviour of origami structures. Using shell elements to model the facets, FEA has been applied to linear-elastic static problems [Liu et al. 15, Gattas and You 15], as well as analyses involving plastic deformations [Ma and You 13, Schenk et al. 14]. The folds are modelled as smooth, bent sections, or by shell elements connected at a fixed angle. The use of FEA can provide insight into the behaviour, but reduced-order models are often preferable for providing a physical understanding. Rigid origami, which represents the folds as hinges, can be augmented with a pseudo-fold across the short diagonal of the facets to represent their bending [Schenk and Guest 11]. The fold lines, representing both facet deformation and folds, can then be given a torsional stiffness. The in-plane deformations are modelled by using bars on the fold lines [Filipov et al. 17]; further fold lines and nodes can be introduced to capture in-plane properties more accurately [Filipov et al. 15]. This bar and hinge model has been extended to non-linear analyses, and a specific implementation, called MERLIN [Liu and Paulino 17], is used in this work for qualitative comparison with FEA.

Evans *et al.* investigate the decay of local perturbations in Miura-ori sheets, using a lattice mechanics approach [Evans et al. 15]. The effect of a local perturbation is related to the unit cell geometry and the magnitude of the actuation, but the decay length is implied to be independent of the fold and facet stiffness properties. Chen *et al*. also describe a strictly geometric dependence of propagation of a local perturbation in a quasi-1D origami strip [Chen et al. 16]. In contrast, the effect of material properties, specifically fold and facet stiffness, on the elastic decay of local actuation is the focus of this paper.

This paper is organised as follows. Section 2 describes the numerical and experimental models used. Section 3 investigates the elastic decay in Miura-ori tubes using a finite element model, and explores the effect of the ratio of the fold and facet stiffness and the unit cell geometry. The paper concludes with a discussion and conclusions in Sections 4 and 5.

2 Numerical & Experimental Model

Three methods are used in the analysis of the Miura-ori tube: (1) an experimental model to provide data for and verify (2) a numerical FEA model for quantitative analysis and (3) MERLIN for a reduced order qualitative analysis.

2.1 Experimental Model

Three separate experiments are detailed: (1) tensile testing of card to determine its in-plane properties, (2) a uniaxial compression of a Miura-ori tube to determine the fold stiffness,

and (3) a local squeezing of a Miura-ori tube, as shown in Figure 1, to provide validation for the numerical models.

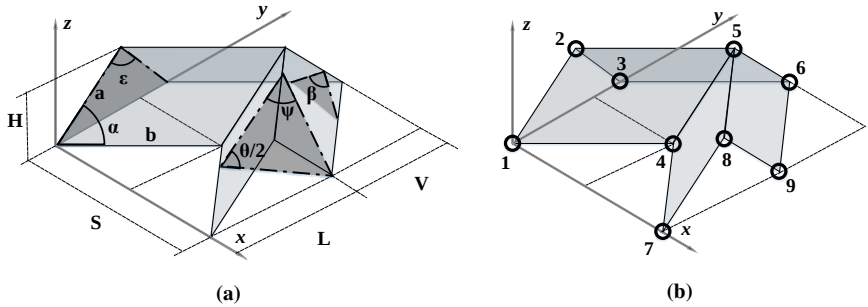

Figure 2: *(a) The geometric parameters of a Miura-ori unit cell; (b) the node numbering system within a unit cell; nodes 2, 5, and 8 on the mirror (negative z) side of the tube are labelled 2M, 5M, and 8M.*

2.1.1 Material and Manufacture

The samples are manufactured using Canford 300 gsm $\pm 5\%$ card, with a thickness of 380 μm $\pm 7.5\%$. The thickness and mass per unit area of the card are measured using multiple calliper measurements (following ASTM D646-13) as 370 μm and 297 gsm respectively, which are both within the manufacturing tolerance. The tensile modulus is measured (following ASTM D828-16), and is orthotropic and bi-linear. The moduli are $E_1 = 2300$ Nmm^{-2} and $E_2 = 6100$ Nmm^{-2} along and perpendicular to the length of the flattened tube respectively. The moduli are constant up to approximately 0.5% strain before transitioning to a lower stiffness up to the failure of the coupon. The initial stiffness is used for the numerical models due to the relatively low strains in the facets. The Poisson's ratios are measured during the same tests and are found to be $\nu_{12} = 0.17$ and $\nu_{21} = 0.4$. The material shear stiffness is estimated following [Jones 67].

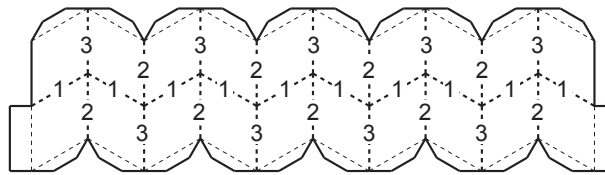

Figure 3: *One of the halves of the Miura tubes that are bonded together. Numbers represent the order of folding.*

The mechanical properties of folds in paper have been investigated on a fold in isolation. Methods include pulling the fold apart [Lechenault et al. 14, Pradier et al. 16, Yasuda et al. 13], pushing the fold together [Abbott et al. 14], or actuating the fold with a known force perpendicular to the material [Francis et al. 13]. Investigations into the effect of folding on the micro-structure of paper show that it delaminates during folding, causing changes in

mechanical properties [Yasuda et al. 13, Beex and Peerlings 09]. This damage has been observed to accumulate over numerous cycles of folding and unfolding [Francis et al. 13, Reid et al. 17]. Therefore, a consistent manufacturing and testing procedure for any experimental samples is important.

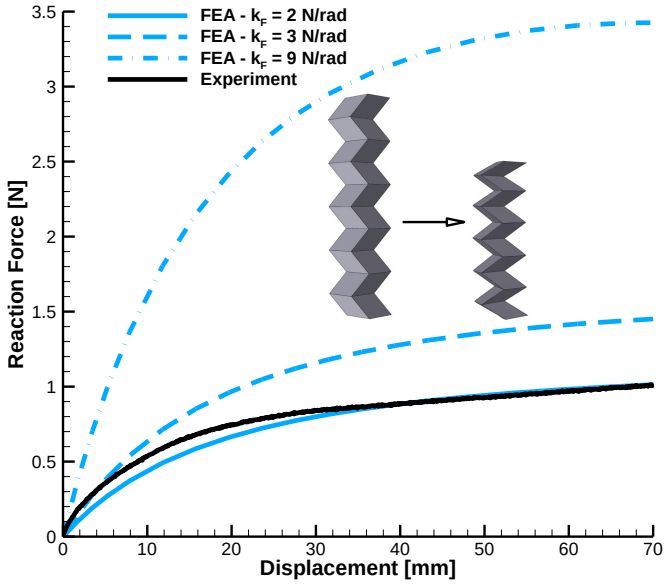

Figure 4: *The experimental results compared against finite element results for a range of fold stiffness values.* $k_F = 2$ N/rad *and* 3 N/rad *are selected as the most appropriate fold stiffness values for comparison with experimental results. However, a single linear fold stiffness cannot capture the entire range of motion.*

The Miura-ori tubes are constructed using the repeating cell shown in Figure 2a. Two mirrored strips, as shown in Figure 3, are cut using a laser cutter with a unit cell characterised by lengths $a = b = 30$ mm and angle $\alpha = 60°$. The fold lines are perforated during the laser cutting; all folds have 2 mm long perforations between 2 mm gaps. Due to the orthotropic nature of the card, the tubes are consistently orientated when they are cut out. Once the halves have been cut, the halves are first pre-creased. The folding follows a predefined sequence, indicated by the numbers in Figure 3. After pre-creasing, the halves are fully compressed and extended in the x-direction before being allowed to rest in their minimum-energy state. The two halves are then bonded together using double sided adhesive tape on the tabs and, finally, fully compressed and fully extended again in the x-direction, before letting the tube assume its rest configuration. The sample is then ready for testing.

2.1.2 Fold Stiffness Measurement

Rather than measuring an individual fold line, the stiffness of the folds is determined from a uniaxial compression test of the Miura-ori tube, where rigid origami kinematics is assumed. The Miura-ori tube is placed between two glass plates, and attached using double sided

adhesive tape on tabs at each end. The glass plates reduce the friction induced as, during uniaxial loading, the cross-sections at the ends deform and rotate. The tubes are globally compressed in the x direction, defined in Figure 2a, at a constant rate of 1 mm/s for 70 mm and the resulting reaction force is recorded, using a 1 kN load cell. The deformation is shown in the schematic inset in Figure 4. The resulting force and displacement data is used to calculate an approximate, averaged linear stiffness of the folds.

The calculation of the fold stiffness is based on the principle of virtual work. To simplify these calculations some assumptions have been used. Firstly, rigid origami assumptions mean that the deformation consists purely of changes in fold angles and these are the same across every unit cell. Further, it is assumed that all folds have the same stiffness and that the folds of the tabs connecting the tube to the glass plates have a negligible contribution to the reaction force. Finally, it is assumed that the tube starts in a zero-energy state and that there are no energy losses in the system. This has been evaluated in literature [Yasuda et al. 13] and is mainly due to high stresses at the vertices. The current experimental and finite element models are not connected at the vertices, thereby reducing the local stress concentrations.

Using these assumptions, the external work and internal strain energy can be equated to find the stiffness of the folds. The external work, U, is a function of the applied force F and displacement ΔS from the initial rest state.

$$U = F\Delta S \tag{1}$$

Taking a constant fold stiffness per unit length, k_F, for all fold lines, the internal strain energy of a single unit cell of the tube is calculated as:

$$U = 2ak_F\Big((\psi-\psi_0)^2+(\beta-\beta_0)^2+(\theta-\theta_0)^2\Big) \tag{2}$$

where ψ_0, β_0, and θ_0 are the angles at the initial rest conditions of the tube, and $a = b$. Differentiating Equations 1 and 2 with respect to S and equating, enables the calculation of the fold stiffness:

$$k_F = \frac{F}{4a\Big((\psi-\psi_0)\frac{d\psi}{dS}+(\beta-\beta_0)\frac{d\beta}{dS}+(\theta-\theta_0)\frac{d\theta}{dS}\Big)} \tag{3}$$

where ψ, β, θ, $d\psi/dS$, $d\beta/dS$, and $d\theta/dS$ are found in terms of S using unit cell kinematics [Schenk and Guest 13, Wei et al. 13].

Using the experimental force and displacement data, a distribution for k_F can be found ranging from 2 to 9 N/rad. An FE analysis of the uniaxial deformation is compared to the experimentally derived force-displacement relationship for different values of linear fold stiffness in Figure 4. A fold stiffness, k_F, between $2-3$ N/rad more closely matches the experimental results over the range of motion; therefore, these are selected for comparison between FEA and experimental local actuations. As all folds are assumed to have the same linear stiffness, it is not possible to derive a relationship between the moment and angle on each fold. Furthermore, Figure 4 shows that a constant fold stiffness cannot accurately describe the entire motion of the compression test. Nonetheless, for small deformations, the constant fold stiffness provides sufficient insight into the structural response of the Miura-ori tube. In future, the stiffness of individual folds will be measured to provide the nonlinear moment-angle relationship for large rotations, as well as study the effect of material fibre direction on the fold stiffness.

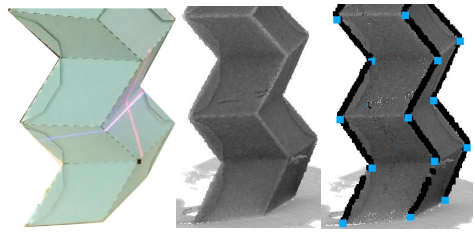

Figure 5: *The local actuation is achieved by using beads attached to nylon wire to compress opposing vertices of the tube. The deformed geometry is captured using a laser scanner, which generates a point cloud that is processed to find the fold lines and vertices.*

2.1.3 Local Actuation

The experimental local actuation tests consist of compressing the unit cell at one end of a tube. This is achieved by pulling together the two central vertices using a pair of beads on a nylon wire. First, a knot is tied in the nylon wire and a bead threaded onto it, before threading the wire through the vertices; this is repeated with another nylon wire and bead from the other side of the tube. The tube is then flattened to its maximum extension in the x-direction, allowed to return to a rest state, and the length measured.

Next, the tube is placed upright, where the x-direction is upwards. The nylon wires are pulled tight to achieve the actuation, in the bottom unit cell, and pinned in place. The outer geometry is captured as a point cloud using a 3D laser scanner, as shown in Figure 5. From this point cloud the folds can be identified by finding the points with the highest and lowest y and z values for a slice along the tube. The average y-position of each fold can then be found. The vertices are found as the points of a fold furthest from the average y-position. The calculated vertices are superimposed onto the point cloud and checked visually. The angle ε is calculated by finding the angle between relevant vectors defined by the vertices. A value for this angle is found for both sides of the tube, which are averaged to give the value for the unit cell. A total of 3 tubes of 10 unit cells were used for the experiments, and each tube was actuated once.

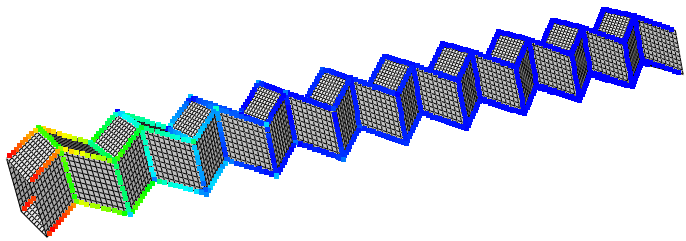

Figure 6: *FEA model of the Miura-ori tube; colours along the fold lines indicate the change in fold angle during actuation.*

2.2 Numerical Models

The FEA model, implemented in ABAQUS/Standard, consists of facets joined together by torsional springs along the fold lines. The facets are meshed using shell elements (S4R). A convergence study found that a mesh density of 25×25 elements on each facet is sufficient to capture the angle ε to within 1% of a mesh with double the elements on each edge, at every point along the tube. A linear-elastic, orthotropic material stiffness is assumed for the paper facets. The torsional springs along the fold lines use hinge elements (CONN3D2) with a linear torsional stiffness; the resulting model is shown in Figure 6. Section 2.1 details how the stiffness properties are determined. Furthermore, a gravity load is included for comparison with experimental results. The tube is constrained such that it is pinned on node 4 and is fixed in the x-direction at nodes 5 and 5M; node numbers are defined in Figure 2b. A displacement in z is prescribed, to move nodes 5 and 5M closer. The initial state of the tube in both the numerical and experimental tests is defined by angle $\theta = 90°$.

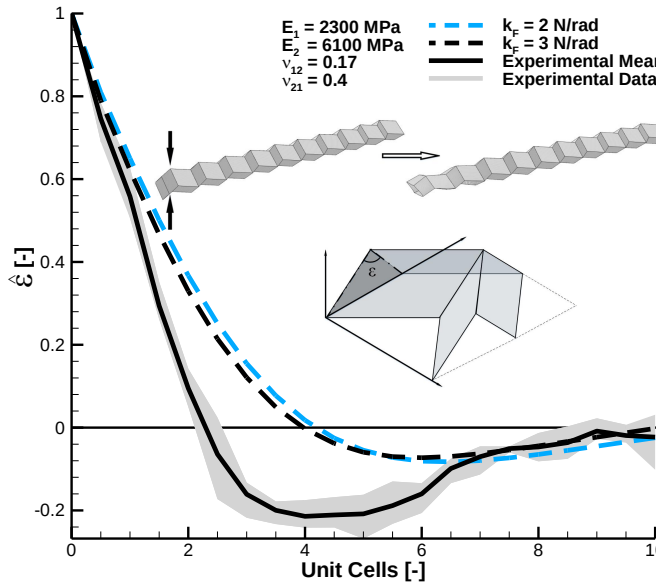

Figure 7: *The angle between the folds reduces along the length of the tube in both the FE analysis and experimental tests. FEA results are shown for different values of fold stiffness. The shaded area indicates the maximum/minimum experimentally determined values.*

All results are normalised using the initial conditions and the maximum value, where ε_0 represents the undeformed configuration:

$$\hat{\varepsilon} = \frac{\varepsilon - \varepsilon_0}{\max(\varepsilon) - \varepsilon_0} \tag{4}$$

Figure 7 shows that the non-linear FEA and experimental tests match closely at the source of actuation and towards the end of the tube, returning to the undeformed shape. Both also

have a negative region which physically represents a deformation in the opposite direction to that of the actuation. This effect, termed a 'spring-back', is discussed further in Section 4. Although gravity accentuates the effect, as shown in Figure 7, it is also present when the effect of gravity is removed; see Figure 8. The global mechanical response is independent of material anisotropy, and is also found with a linear analysis. The linear approximation is valid up to an actuation compressing the tube by 3/4 of its initial height H, with analyses at compressions of $H/4$ and $H/2$ showing the same normalised response. Therefore, an actuation of $H/4$ is used for further analyses. The reduced-order MERLIN model also captures the behaviour; a qualitative comparison is shown in Figure 8 as representative stiffness and area values have not been established for MERLIN.

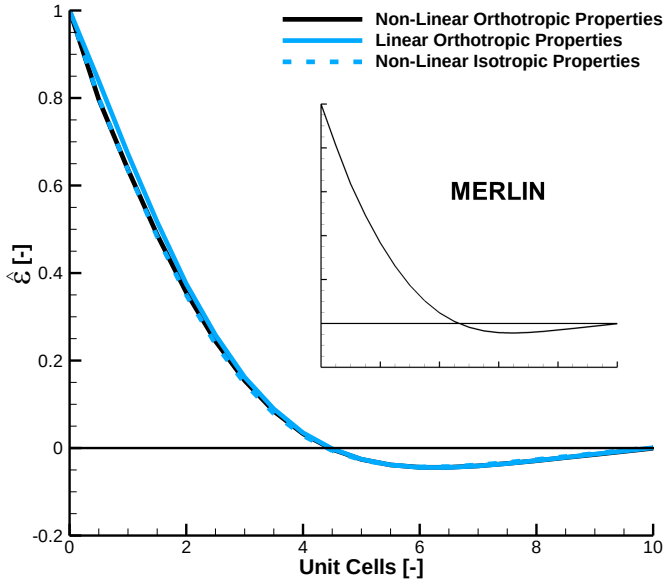

Figure 8: *The behaviour of the tube in response to local actuation can be effectively captured with isotropic material properties and a linear FE analysis. Actuating the unit cell with a $H/2$ displacement shows a nominally identical response using linear and non-linear analyses. For a $3H/4$ actuation the linear and non-linear responses start to diverge. The reduced-order non-linear MERLIN model (inset with an axes range equal to the main plot) also captures the behaviour.*

Despite these similarities, the 'spring-back' effect is greater in the experimental results, which could be due to differing stiffness in each fold. As highlighted in Section 2.1, the card material is orthotropic, and the fold stiffness will depend on the orientation of the fold with respect to that of the card. Future work will test single folds in isolation to characterise this effect. Nonetheless, despite the difference in magnitude of the 'spring-back' in the experimental and numerical tests, the important features of the behaviour are captured in the FEA model. Consequently, it is used to further investigate the behaviour of the Miura-ori tubes.

3 Elastic Decay in Miura tubes

The FEA model is used to investigate the effect of (1) the elastic stiffness properties and (2) unit cell geometry (thickness, size, facet angle) on the local actuation of an origami tube. In the following analyses, the orthotropic nature of the paper is neglected, and gravity is removed. The effective, isotropic Young's modulus is taken as $E = \sqrt{E_1 E_2} = 3750$ MPa and effective isotropic Poisson's ratio is taken as $\nu = \sqrt{\nu_{12}\nu_{21}} = 0.261$.

3.1 Elastic Properties

Two key material parameters in the mechanical response of origami structures are the fold stiffness and facet bending stiffness [Schenk and Guest 11]. Rather than specifying the fold stiffness directly, we make use of a length scale L^* introduced by [Lechenault et al. 14],

$$L^* = \frac{B}{k_F} \quad \text{where} \quad B = \frac{Et^3}{12(1-\nu^2)} \tag{5}$$

which relates the fold stiffness k_F, per unit length of fold, to the material flexural stiffness B. L^* provides a compact measure of the ratio between the mechanical properties of the facets and folds, to characterise the overall behaviour of the origami structure. Larger values of L^* correspond to an origami system that is closer to rigid origami, with perfect hinges and rigid facets.

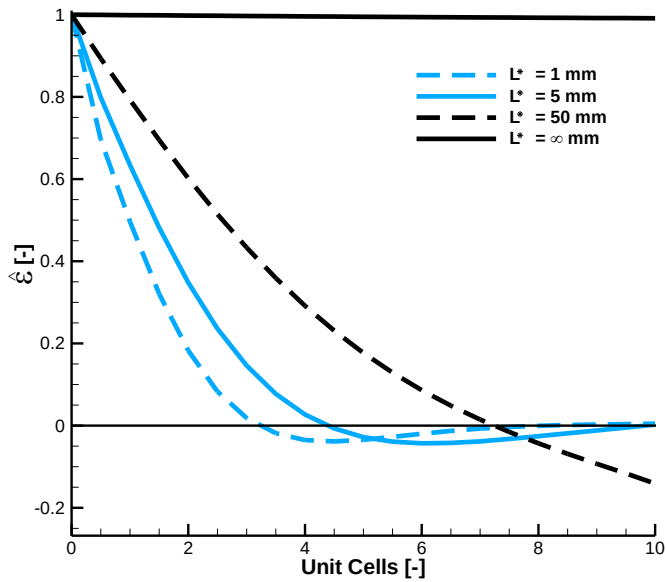

Figure 9: *Reducing L^* causes a reduction in the decay length, as the folds become stiffer in comparison to the facets. In all cases $a = b = 30$ mm, $\alpha = 60°$, $t = 0.37$ mm, and $\theta = 90°$.*

Figure 9 shows FEA models with varying length scales; L^* is varied by changing the fold stiffness and keeping the material properties and geometry of the facets constant. Included is

a model with perfect hinges, leading to an infinite L^*, which behaves as rigid origami and has a negligible elastic decay. Conversely, smaller length scales show an increased localisation of the actuation, as the bending stiffness of the facets reduces. However, for analyses where the actuation completes within the length of the tube, the magnitude of any 'spring-back' remains approximately constant. For the test with $L^* = 50$ mm the decay does not complete within the length of the tube, which results in a significant change in the response of the structure. The role of edge effects on decay length will be explored in future work. When the local actuation of a Miura-ori strip (one half of the tube) is investigated, the effect is no longer observed. This suggests that the 'spring-back' phenomenon is a result of the implied boundary condition of symmetry about a central $x-y$ plane in the tube, which is not present in the strip. The implications of this are discussed further in Section 4.

3.2 Unit Cell Geometry

A limitation of the length scale is that it does not account for the facet geometry, and therefore does not effectively capture the facet bending stiffness. The facet stiffness is here taken as the equivalent stiffness of a pseudo-fold across the short diagonal, k_B. [Filipov et al. 17] provide an empirical formulation for the bending stiffness per unit length, k_B, of a facet

$$k_B = \left(0.55 - 0.42\frac{\Sigma\gamma}{\pi}\right) B \left(\frac{1}{tD_s^2}\right)^{1/3} \tag{6}$$

where D_s is the shortest diagonal length, t the material thickness, B the material flexural stiffness, and $\Sigma\gamma$ is the sum of the exterior angles of the facet. For the parallelogram facets considered here, this equals 2α, where α is defined in Figure 2a.

The ratio of the fold and facet bending stiffness k_B/k_F has previously been used to characterise the mechanical response of origami systems [Schenk and Guest 11].

$$\eta = \frac{k_B}{k_F} = \frac{E}{12k_F(1-\nu^2)}\left(0.55 - 0.42\frac{2\alpha}{\pi}\right)\left(\frac{t^4}{D_s}\right)^{2/3} \tag{7}$$

Equation 7 captures the fold stiffness, elastic material properties, and facet geometry as a product of the effect of material and geometric properties. If the in-plane (E) and fold stiffness (k_F) are changed proportionally to maintain a constant η identical behaviour is observed for significantly different stiffness values, for a fixed geometry.

However, varying the facet geometry will affect the elastic decay. Figure 10 shows the effect of changing facet dimensions and parallelogram angle, while maintaining a constant ratio $D_s/t = 81$, a constant $\eta = 0.15$, and a constant initial configuration θ. In contrast to the elastic properties, the geometry of the unit cell has a more complicated effect, which is not fully captured by the formulation in Equation 7. Nonetheless, the salient features, localisation of actuation in origami with finite facet stiffness and a 'spring-back' effect, are shown not to be specific to a particular geometry.

The ratio between the material flexural stiffness of the facets and the elastic stiffness of the folds can be used to describe the decay of localised actuation in Miura-ori tubes of fixed geometry. However, the unit cell geometry also affects the elastic decay and Equation 7 does not adequately capture this relationship. Future work will aim to better capture this dependence on the unit cell geometry in order to develop a formulation to describe the elastic decay of localised actuation in Miura-ori tubes.

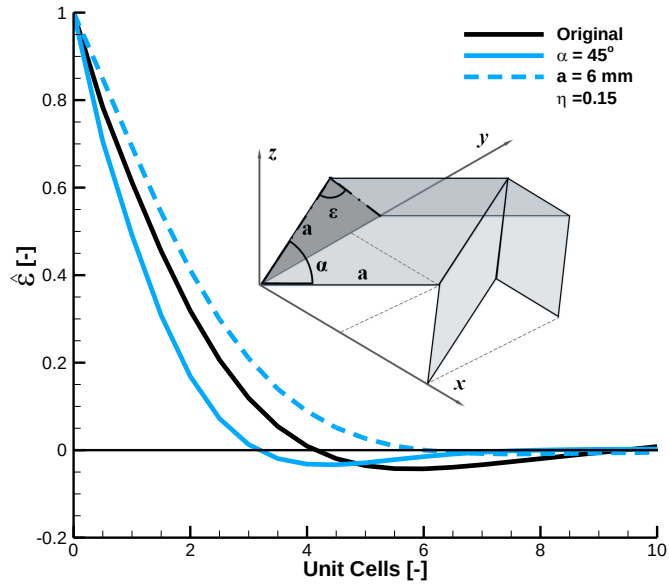

Figure 10: *The behaviour of the decay is sensitive to both the unit cell shape and size. The original comparison FEA test has* $a = 30$ mm *and* $\alpha = 60^\circ$ *and all of the tests have* $D_s = 81t$*, which is identical to the experimental tests. Changes to* α *and a are with the other parameter kept constant at the original value;* k_F *is also changed to maintain a constant* $\eta = 0.15$*.*

4 Discussion

Numerical and experimental results show a good correlation, as shown in Figure 7; however, the experimental measurements exhibit a greater magnitude of 'spring-back'. The reason for this discrepancy is not currently understood. The magnitude of the 'spring-back' is shown to be insensitive to small changes in fold stiffness. Therefore, the effects of variations in fold stiffness due to orientation with respect to the grain of the card, or due to the non-linear stiffness of the fold lines, are not expected to be significant. Investigating the causes of this difference will be the subject of future work.

This unexpected 'spring-back' behaviour in the Miura-ori tube invites an analogy with the response of a long thin-walled cylinder to an applied ring load, where the deflection decays in an oscillatory fashion away from the point of application [Calladine 83]. That analysis is itself analogous to that of a beam on an elastic foundation [Hartog 52]. For the thin-walled cylinder the elastic foundation is provided by the generated hoop stress. In the Miura-ori tubes the facets also experience in-plane strains, which provide the elastic foundation for the 'spring-back' in the elastic decay. Initial work suggests that the decay curves in the Miura-ori tube can be closely approximated by the equations for a beam on elastic foundation, and future work will aim to characterise this behaviour analytically.

The effect of in-plane and fold/facet stiffness on the localised actuation response is not limited to Miura-ori tubes. Figure 11 shows the effect of local actuation of a single unit cell

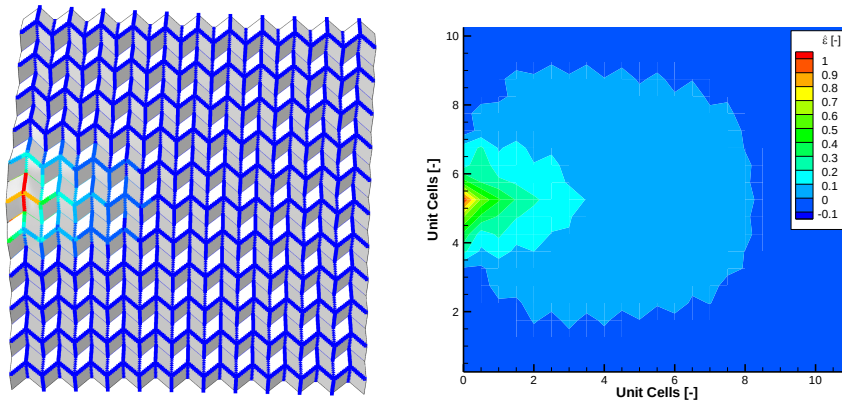

(a) **(b)**

Figure 11: *(a) a single unit cell of a Miura-ori sheet is actuated; colours indicate the change in fold angle throughout the sheet; (b) the change in angle $\hat{\varepsilon}$ again shows a spring-back effect, where unit cells have an oppositely signed deformation to the original actuation.*

in a large (11×11) Miura-ori sheet; all folds in the unit cell are opened simultaneously. The finite facet stiffness results in a localisation of the actuation, and a 'spring-back' effect is again observed. Here, the sheet around the actuated unit cell provides the elastic foundation. Similar to the Miura-ori tubes, changing the elastic properties of the folds and facets in a Miura-ori sheet causes a different profile of decay. This is in contrast to previous work on inhomogeneous deformations [Evans et al. 15] which suggests that the decay of a local perturbation depends only on the geometry of a unit cell, the initial conditions of the sheet, and the size of the perturbation.

5 Conclusions

This paper investigates the effect of the elastic properties of the facets and folds of Miura-ori tubes on the elastic decay of a localised actuation. This is done numerically using a Finite Element model, which is verified experimentally against paper samples.

Elastic properties representing a larger departure from idealised rigid origami lead to increasing localisation of an actuation. For a given geometry this effect can be described by the ratio of the in-plane stiffness of the facets and the torsional stiffness of the folds. This behaviour is linear for small actuations and is not influenced by the orthotropic material properties of paper. Furthermore, a new phenomenon in origami has been observed: a 'spring-back' effect where a local actuation causes a deformation of the opposite sense at a point elsewhere in the system. This effect is not specific to Miura-ori tubes and has also been observed in a Miura-ori sheet.

Data Statement

All supporting data are provided within this paper.

Acknowledgments

This work was supported by the Engineering and Physical Sciences Research Council through the EPSRC Centre for Doctoral Training in Advanced Composites for Innovation and Science (grant number EP/L016028/1).

References

[Abbott et al. 14] A. C. Abbott, P. R. Buskohl, J. J. Joo, G. W. Reich, and R. A. Vaia. "Characterization of creases in polymers for adaptive origami structures." In *ASME 2014 Conference on Smart Materials, Adaptive Structures and Intelligent Systems*, 2014.

[Beex and Peerlings 09] L. A. A. Beex and R. H. J. Peerlings. "An experimental and computational study of laminated paperboard creasing and folding." *International Journal of Solids and Structures* 46:24 (2009), 4192–4207.

[Calladine 83] C. R. Calladine. *Theory of Shell Structures*. New York: Cambridge University Press, 1983.

[Chen et al. 16] Bryan Gin-ge Chen, Bin Liu, Arthur A. Evans, Jayson Paulose, Itai Cohen, Vincenzo Vitelli, and C. D. Santangelo. "Topological Mechanics of Origami and Kirigami." *Physical Review Letters* 116:13 (2016), 135501.

[Dudte et al. 16] L. H. Dudte, E. Vouga, T. Tachi, and L. Mahadevan. "Programming curvature using origami tessellations." *Nature Materials* 15:5 (2016), 583–588.

[Evans et al. 15] A. A. Evans, J. L. Silverberg, and C. D. Santangelo. "Lattice mechanics of origami tessellations." *Physical Review E* 92:1 (2015), 013205.

[Filipov et al. 15] E.T. Filipov, T. Tachi, and G. H. Paulino. "Origami tubes assembled into stiff, yet reconfigurable structures and metamaterials." *Proceedings of the National Academy of Sciences* 112:40 (2015), 12321–12326.

[Filipov et al. 17] E. T. Filipov, K. Liu, T. Tachi, M. Schenk, and G. H. Paulino. "Bar and hinge models for scalable analysis of origami." *International Journal of Solids and Structures* 124 (2017), 26–45.

[Francis et al. 13] K. C. Francis, J. E. Blanch, S. P. Magleby, and L. L. Howell. "Origami-like creases in sheet materials for compliant mechanism design." *Mechanical Sciences* 4:2 (2013), 371–380.

[Gattas and You 15] J.M. Gattas and Z. You. "The behaviour of curved-crease foldcores under low-velocity impact loads." *International Journal of Solids and Structures* 53 (2015), 80–91.

[Hartog 52] J. P. Den Hartog. *Advanced Strength of Materials*. New York: McGraw-Hill Book Company Inc., 1952.

[Jones 67] A. R. Jones. "An experimental investigation of in-plane elastic moduli of paper." Ph.D. thesis, Lawrence University, 1967.

[Lechenault et al. 14] F. Lechenault, B. Thiria, and M. Adda-Bedia. "Mechanical response of a creased sheet." *Physical Review Letters* 112:24 (2014), 1–5.

[Liu and Paulino 17] K. Liu and G. H. Paulino. "Nonlinear mechanics of non-rigid origami: an efficient computational approach." *Proceedings of the Royal Society A: Mathematical, Physical and Engineering Science* 473:2206 (2017), 20170348.

[Liu et al. 15] S. Liu, G. Lu, Y. Chen, and Y. W. Leong. "Deformation of the Miura-ori patterned sheet." *International Journal of Mechanical Sciences* 99 (2015), 130–142.

[Ma and You 13] Ji. Ma and Z. You. "Energy Absorption of Thin-Walled Square Tubes With a Prefolded Origami Pattern–Part I: Geometry and Numerical Simulation." *Journal of Applied Mechanics* 81:1 (2013), 011003.

[Pradier et al. 16] C. Pradier, J. Cavoret, D. Dureisseix, C. Jean-Mistral, and F. Ville. "An Experimental Study and Model Determination of the Mechanical Stiffness of Paper Folds." *Journal of Mechanical Design* 138:4 (2016), 041401.

[Reid et al. 17] A. Reid, F. Lechenault, S. Rica, and M. Adda-Bedia. "Geometry and design of origami bellows with tunable response." *Physical Review E* 95:1 (2017), 013002.

[Schenk and Guest 11] M. Schenk and S. D. Guest. "Origami Folding: A Structural Engineering Approach." In *Origami 5: Fifth International Meeting of Origami Science, Mathematics, and Education*, pp. 291–304, 2011.

[Schenk and Guest 13] M. Schenk and S. D. Guest. "Geometry of Miura-folded metamaterials." *Proceedings of the National Academy of Sciences* 110:9 (2013), 3276–3281.

[Schenk et al. 14] M. Schenk, S. D. Guest, and G. J. McShane. "Novel stacked folded cores for blast-resistant sandwich beams." *International Journal of Solids and Structures* 51:25-26 (2014), 4196–4214.

[Silverberg et al. 15] J. L. Silverberg, J. Na, A. A. Evans, B. Liu, T. C. Hull, C. D. Santangelo, R. J. Lang, R. C. Hayward, and I. Cohen. "Origami structures with a critical transition to bistability arising from hidden degrees of freedom." *Nature materials* 14:4 (2015), 389–93.

[Tachi 09] T. Tachi. "Simulation of Rigid Origami." In *Origami 4*, pp. 175–187. A K Peters/CRC Press, 2009.

[Wei et al. 13] Z. Y. Wei, Z. V. Guo, L. Dudte, H. Y. Liang, and L. Mahadevan. "Geometric mechanics of periodic pleated origami." *Physical Review Letters* 110:21 (2013), 1–5.

[Yasuda et al. 13] H. Yasuda, T. Yein, T. Tachi, K. Miura, and M. Taya. "Folding behaviour of Tachi-Miura polyhedron bellows." *Proceedings of the Royal Society A: Mathematical, Physical and Engineering Sciences* 469:2159.

Steven Grey
Bristol Composites Institute (ACCIS), Department of Aerospace Engineering, University of Bristol, Bristol, BS8 1TR, United Kingdom, e-mail: steven.grey@bristol.ac.uk

Fabrizio Scarpa
Bristol Composites Institute (ACCIS), Department of Aerospace Engineering, University of Bristol, Bristol, BS8 1TR, United Kingdom, e-mail: f.scarpa@bristol.ac.uk

Mark Schenk
Bristol Composites Institute (ACCIS), Department of Aerospace Engineering, University of Bristol, Bristol, BS8 1TR, United Kingdom, e-mail: m.schenk@bristol.ac.uk